

# PROCEEDINGS OF SPIE

[SPIDigitalLibrary.org/conference-proceedings-of-spie](https://spiedigitallibrary.org/conference-proceedings-of-spie)

## Very high resolution spectro-interferometry with wavefront sensing capabilities on Subaru/SCEXAO using photonics

Vievard, S., Ahn, K., Arriola, A., Barjot, K., Cvetojevic, N., et al.

S. Vievard, K. Ahn, A. Arriola, K. Barjot, N. Cvetojevic, V. Deo, T. Gretzinger, S. Gross, O. Guyon, E. Huby, N. Jovanovic, T. Kotani, S. Lacour, T. Lagadec, M. Lallement, V. Lapeyrere, J. Lozi, F. Marchis, G. Martin, M.-A. Martinod, B. Norris, G. Perrin, D. Rouan, N. Skaf, P. Tuthill, M. Withford, G. Duchêne, "Very high resolution spectro-interferometry with wavefront sensing capabilities on Subaru/SCEXAO using photonics," Proc. SPIE 11823, Techniques and Instrumentation for Detection of Exoplanets X, 118230C (1 September 2021); doi: 10.1117/12.2594840

**SPIE.**

Event: SPIE Optical Engineering + Applications, 2021, San Diego, California, United States

# Very high angular resolution spectro-interferometry with wavefront sensing capabilities on Subaru/SCEXAO using photonics

S. Vievard<sup>a,b</sup>, K. Ahn<sup>a</sup>, A. Arriola<sup>c</sup>, K. Barjot<sup>d</sup>, N. Cvetojevic<sup>e</sup>, V. Deo<sup>a</sup>, G. Duchène<sup>f</sup>, T. Gretzinger<sup>c</sup>, S. Gross<sup>c</sup>, O. Guyon<sup>a,b,g</sup>, E. Huby<sup>d</sup>, N. Jovanovic<sup>h</sup>, T. Kotani<sup>b</sup>, S. Lacour<sup>d</sup>, T. Lagadec<sup>i</sup>, M. Lallement<sup>a,d</sup>, V. Lapeyrere<sup>d</sup>, J. Lozi<sup>a</sup>, F. Marchis<sup>j</sup>, G. Martin<sup>k</sup>, M.-A. Martinod<sup>l,m,n</sup>, B. Norris<sup>l,m,n</sup>, G. Perrin<sup>d</sup>, D. Rouan<sup>d</sup>, N. Skaf<sup>a,d,o</sup>, P. Tuthill<sup>l,m,n</sup>, and M. Withford<sup>c</sup>

<sup>a</sup>Subaru Telescope, National Astronomical Observatory of Japan, National Institutes of Natural Sciences (NINS), 650 North A'ohōkū Place, Hilo, HI, 96720, U.S.A.

<sup>b</sup>Astrobiology Center of NINS, 2-21-1, Osawa, Mitaka, Tokyo, 181-8588, Japan

<sup>c</sup>MQ Photonics Research Centre, Macquarie University, Sydney, Australia

<sup>d</sup>LESIA, Observatoire de Paris, 5 place Jules Janssen, 92195 Meudon, France

<sup>e</sup>Observatoire de la Côte d'Azur, 96 Boulevard de l'Observatoire, 06300 Nice, France

<sup>f</sup>Department of Astronomy, University of California at Berkeley, Berkeley, CA 94720-3411

<sup>g</sup>College of Optical Sciences, University of Arizona, Tucson, AZ 85721, U.S.A.

<sup>h</sup>California Institute of Technology, 1200 E California Blvd, Pasadena, CA 91125, U.S.A.

<sup>i</sup>Research School of Astronomy and Astrophysics, Australian National University

<sup>j</sup>Carl Sagan Center at the SETI Institute, 189 Bernardo Av., Mountain View, CA 94043, USA

<sup>k</sup>Univ. Grenoble Alpes, CNRS, IPAG, 38000 Grenoble, France

<sup>l</sup>Sydney Institute for Astronomy, School of Physics, The University of Sydney, NSW 2006, Australia

<sup>m</sup>Sydney Astrophotonic Instrumentation Laboratories, Physics Road, University of Sydney, NSW 2006, Australia

<sup>n</sup>AAO-USyd, School of Physics, University of Sydney 2006

<sup>o</sup>Department of Physics and Astronomy, University College London, London, United Kingdom

## ABSTRACT

Post Extreme Adaptive-Optics (ExAO) spectro-interferometers design allows high contrast imaging with an inner working angle down to half the theoretical angular resolution of the telescope. This regime, out of reach for conventional ExAO imaging systems, is obtained thanks to the interferometric recombination of multiple sub-apertures of a single telescope, using single mode waveguides to remove speckle noise. The SCEXAO platform at the Subaru telescope hosts two instruments with such design, coupled with a spectrograph. The FIRST instrument operates in the Visible (600-800nm, R 400) and is based on pupil remapping using single-mode fibers. The GLINT instrument works in the NIR (1450-1650nm, R 160) and is based on on-chip nulling interferometry. We present here how these photonic instruments have the unique capability to simultaneously do high contrast imaging and be included in the wavefront sensing architecture of SCEXAO.

**Keywords:** Interferometry, Pupil remapping, Single-mode fibers, photonics, high contrast imaging, high angular resolution, wavefront sensing, island effect

## 1. INTRODUCTION

Since the first detection in 1995,<sup>1</sup> more than 5000 exoplanets were discovered. The techniques used to achieve these discoveries are qualified either as indirect (e.g. radial velocity, transit) or direct imaging. The latter consists in masking the light of a star in the focal plane, using a coronagraph, in order to reveal its circumstellar environment. About 20 exoplanets were imaged thanks to coronagraphs, at a distance relatively large from their host star ( $\geq 20$  Astronomical Units). The reason for this is that the Inner Working Angle (IWA) of coronagraphs

---

Further author information: Sebastien Vievard: E-mail: vievard@naoj.org

is  $2\lambda/D$  with  $\lambda$  the wavelength and  $D$  the telescope diameter. For an 8-meter class telescope, this corresponds to about 70mas at 1550nm.

The key scientific objectives of imaging exoplanets is to understand how they form and evolve, what their atmosphere composition is, and assess whether they can host life or not. Technical requirements to answer these questions are :

- High contrast : exoplanets are extremely less bright than their host star by a factor of respectively  $10^{-6}$  and  $10^{-9}$  for hot Jupiters and Earth-like planets.<sup>2</sup>
- High angular resolution : exoplanets are close from their host stars. Studies showed that there is a high abundance of massive planets about 1 to 5 AU from their host star (in the case of Sun-like host stars).<sup>3</sup> In the case of the Taurus group, the closest stellar formation region from Earth (140 parsec), this corresponds to an angular distance of 7 to 40mas. The challenge here is that this region of interest is out of reach for current 8-meter telescope using coronagraphs.

One solution to overcome the angular resolution limitation, using an 8-meter class telescopes, is to do single telescope interferometry. Sparse Aperture Masking (SAM)<sup>4</sup> consists in placing a non-redundant mask in a pupil plane of the telescope and recombining the coherent light from each sub-pupil. The non-redundancy of the mask allows for each baseline (vector defined by each pair of sub-pupils) to be unique. In the Fourier domain, it means that each baseline spatial frequency is independently retrieved. The advantage of this technique is that the spatial resolution is *at least*  $0.5\lambda/B_{max}$ , with  $B_{max}$  the interferometer longest baseline. Considering  $B_{max}$  as the diameter of the telescope, SAM allows to beat the single telescope diffraction limit, and allows to have a region of interest that can potentially go down to 10mas or less, on an 8-meter telescope. The drawbacks of using SAM are that 1- it can only exploit a fraction of the pupil because of the non-redundancy requirement, and 2- remaining speckle noise over each sub-pupil limits the achievable contrast to about  $10^{-3}$ .<sup>4</sup>

Three technical solutions can help dealing with SAM drawbacks. First, the pupil remapping technique<sup>5</sup> which consists in reformatting a redundant sub-pupil configuration into a non-redundant one using single mode fibers (SMFs). This theoretically allows to use the whole pupil by dividing all of it into sub-pupils, and re-arrange them in a non-redundant configuration. Second, the use of SMFs allows to 'clean' the wavefront, getting rid of speckle noise over each sub-pupil. Due to the physical properties of an SMF, a corrugated wavefront injected into it will be flat at the output. Finally, the two can be combined into an integrated optic chip.<sup>6</sup> These devices can have engraved single mode waveguides and allow to perform individual recombination of each sub-pupil pair. An advantage compared to the sole use of single mode fibers is that it can be extremely compact (smaller than a credit card cut in half).

The Subaru Coronagraphic Extreme Adaptive Optics<sup>7</sup> (SCEExAO) platform hosts two single aperture interferometers coupled with a spectrograph : FIRST in the 600-800nm wavelength range (R 400) and GLINT in the 1450-1650nm wavelength range (R 160). They both sample the pupil, and aim at injecting the beams into single mode waveguides. In the second section of this paper, we present each instrument concept and setup. In the third section, we present how these instrument were exploited on-sky to deliver measurements below de diffraction limit of the Subaru Telescope. Finally we show in the fourth section that both instrument also have wavefront sensing capabilities that can be used to improve the achievable contrast of any high contrast imaging instruments.

## 2. INSTRUMENT DESCRIPTION

In this section we describe the SCEExAO instrument, then we present the FIRST and GLINT principle and setup.

### 2.1 The SCEExAO instrument

SCEExAO is a versatile platform dedicated to high contrast imaging on the Subaru Telescope. Located at the Nasmyth Infra-Red focus, it gets a partially corrected wavefront from the adaptive optics facility AO188.<sup>8</sup> In its essence, SCEExAO is composed by 1- a pyramid wavefront sensor<sup>9</sup> operating in the Visible (around 800 – 950 nm) and delivering a wavefront quality over 80% Strehl (in H-band) 2- several coronagraphs to suppress star light

and reveal/study close circumstellar environment. Over the last 10 years SCExAO complexity increased and it now hosts several science<sup>7,10,11</sup> and experimental modules including GLINT and FIRST. The various modules are distributed between two optical benches: an IR (950nm – 2.5μm) and a Visible (600 – 950 nm) bench (see Fig. 1).

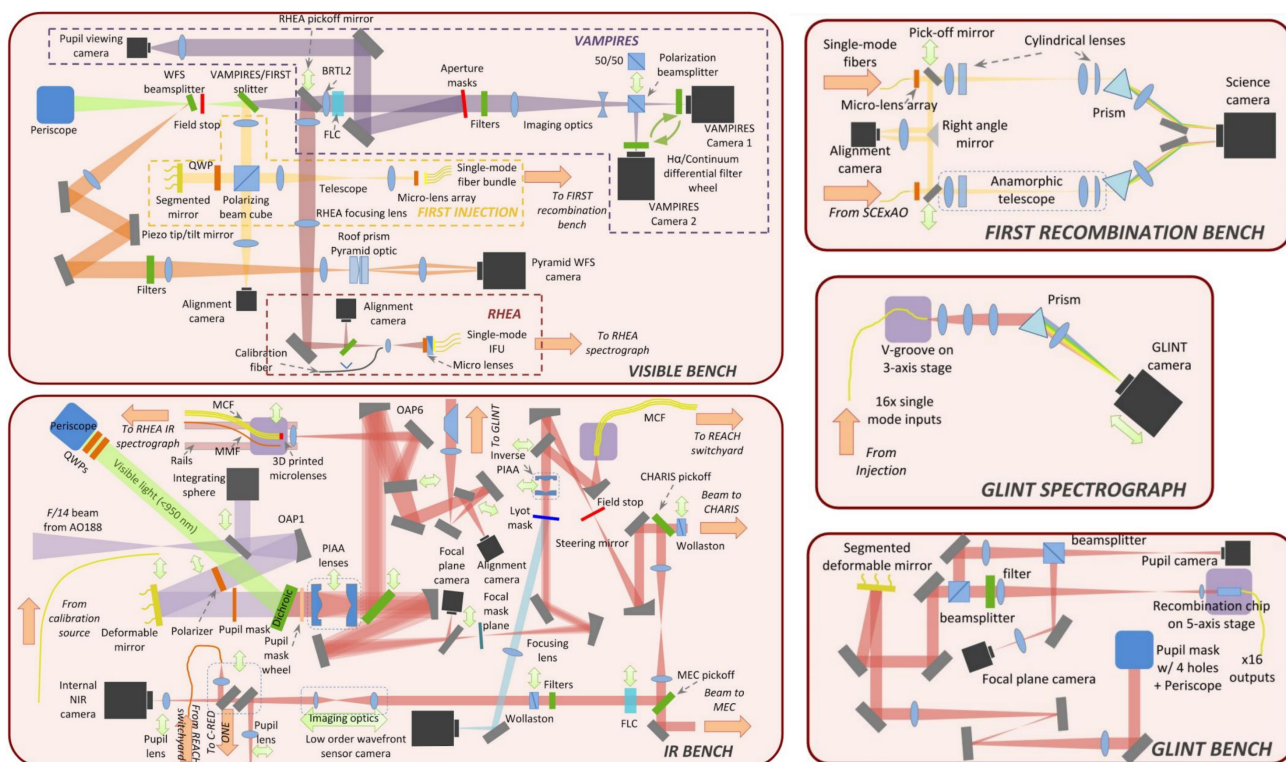


Figure 1. SCExAO schematic diagram. SCExAO is divided in two benches : an IR one and a Visible one. GLINT and FIRST injection benches respectively sit on the IR and the Visible bench. Fibers are used to bring GLINT and FIRST light signal from the injection respectively to the spectrograph and recombination benches.

## 2.2 The FIRST instrument

FIRST<sup>12</sup> (Fibred Imager for a Single Telescope) uses SMFs to combine pupil remapping and spatial filtering. Fig. 2 shows the principle of the instrument. The pupil of the telescope is sampled thanks to a 2D micro-lens array positioned in a pupil plane. Each sub-pupil is injected into a SMF. The optimization of the injection is performed by an Iris AO segmented MEMS, whose segments are individually conjugated with a micro-lens. All the SMFs are contained into a fiber bundle. Each SMF is connected at the other end to extension SMFs that run to the recombination bench. On the recombination bench, the extension fibers are connected to SMFs that end in a 1D V-groove. A total of 18 sub-pupils are currently exploited in 2 sets of 9 fibers. Each set ends in its own V-groove in a non-redundant pattern. Therefore, for each set of fibers, the 9 redundant baselines from the input pupil are now 9 non-redundant baselines corresponding to 36 different spatial frequencies.

The outputs of each fibers are collimated and then are either recombined and spectrally dispersed with an equilateral SF2-prism, or re-imaged on a camera for injection optimization. In order to increase the spectral resolution, an afocal anamorphic system, consisting in cylindrical lenses, stretches the beam in the dispersion direction and compresses it in the orthogonal direction. The acquired fringe pattern contains information in terms of Optical Path Difference (OPD) and in terms of spectrum (wavelength,  $\lambda$ ). The spectral resolution obtained is empirically around 300 @700nm.

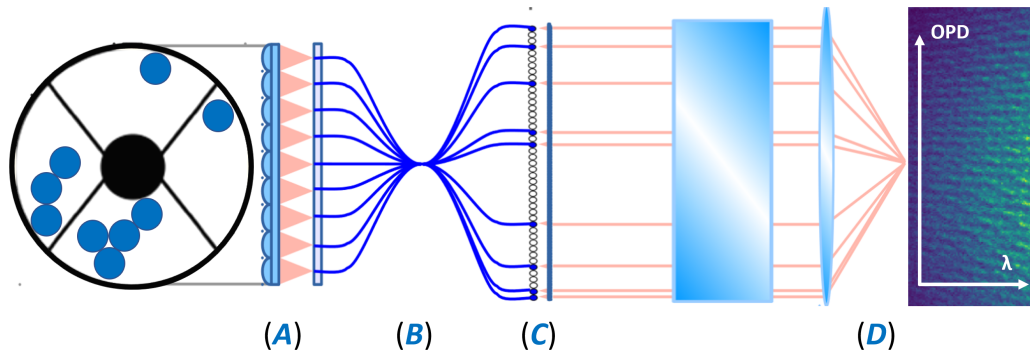


Figure 2. FIRST instrument principle: the pupil of the telescope is divided into several sub-apertures (A). The sub-apertures are injected into a single-mode fibers (B) and re-arranged into a non-redundant pattern (C). The interferometric signal obtained after recombination is dispersed allowing to have Optical Path Difference (OPD) information as a function of the wavelength (D).

### 2.3 The GLINT instrument

GLINT<sup>13</sup> (Guided-Light Interferometric Nulling Technology) samples the pupil using a non-redundant 4-apertures opaque carbon fibre mask. Each of the sub-pupil is conjugated downstream with an Iris AO segmented MEMS, then with micro-lenses, in order to optimally inject the signal into the single-mode waveguides of a chip. Between the MEMS and the micro-lens array, a polarizer selects a single linear polarization and a dichroic splits the beam between the science path and the alignment path for the pupil mask and the MEMS. The integrated optics chip is the core element of GLINT. It is composed by two parts (see Fig. 3) : first, the pupil remapping part re-formats the sub-pupil configuration from 2D to 1D. Second, the nuller part recombines the sub-pupils pairwise and provides photometric outputs. From 4 sub-apertures inputs in the chip, we then get 16 outputs :

- 4 photometric (P) channels,
- 6 *null outputs* (N) : containing the destructive interferences from 6 baselines,
- 6 *anti-null outputs* (AN) : containing the constructive interferences from 6 baselines.

Each output is individually fed to the spectrograph via 16 separate SMFs. The spectrally dispersed beams are imaged on a C-Red2 InGaAs camera.<sup>14</sup> We show an image example Fig. 4.

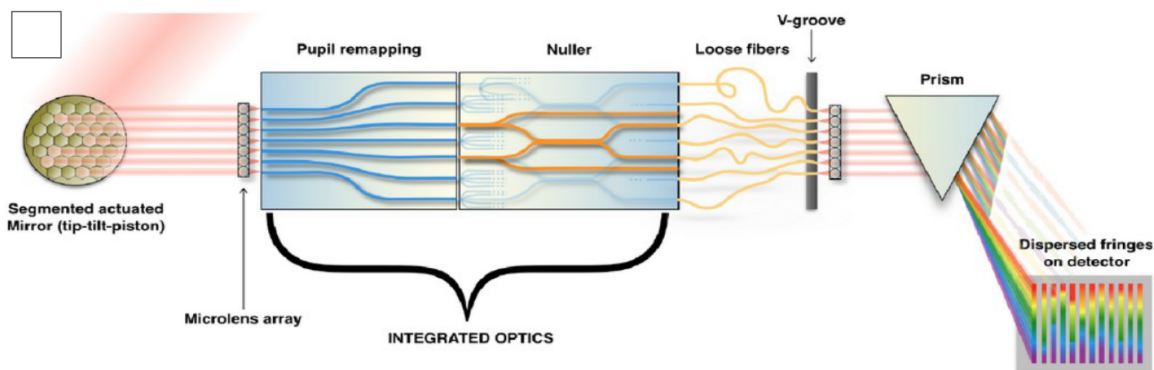


Figure 3. GLINT instrument principle:<sup>15</sup> the telescope pupil is sampled in 4 sub-pupils. Each sub-pupil is directly injected into an integrated optics chip thanks to a micro-lens array. The chip is divided in two parts : the remapping part and the nuller part. Each output is then connected to a V-groove, collimated and imaged on a detector after spectral dispersion.

### 3. SCIENCE BELOW THE TELESCOPE DIFFRACTION LIMIT WITH SINGLE TELESCOPE INTERFEROMETERS

#### 3.1 Science with FIRST

We showed on Fig. 2 a typical image acquired with FIRST. Because the baselines are very compact, a well suited technique to extract information from the fringes is to use the fringe fitting technique.<sup>16</sup> FIRST data reduction is extensively described in previous publications,<sup>12,17</sup> therefore we will not go into much details here. The goal of the fringe fitting technique is to estimate the complex coherence terms ( $\mu_{nn'}$ ) for each baseline ( $n - n'$ ) from the fringe pattern. It writes as:

$$\mu_{nn'} = |V_{nn'}| e^{i\psi_{nn'}} A_n A_{n'} e^{i\Delta\Phi_{nn'}}. \quad (1)$$

$|V_{nn'}|$  and  $\psi_{nn'}$  are respectively the object's complex visibility modulus and phase.  $A_n$ ,  $A_{n'}$  and  $\Delta\Phi_{nn'}$  are respectively sub-pupils  $n$  and  $n'$  flux and differential piston. The main goal of the data reduction pipeline is to provide spatial and spectral information about resolved objects (*e.g.* stellar binaries or giant stars). This information is contained in the object's complex visibilities. The way to extract the latter is through closure phase (CP) measurements, which are by definition the phase of the bispectrum  $\mu_{nn'n''}$ :

$$\mu_{nn'n''} = \langle \mu_{nn'} \mu_{n'n''}^* \mu_{n''n'}^* \rangle, \quad (2)$$

where  $n$ ,  $n'$  and  $n''$  are the sub-pupil indexes used to form the triangle and  $\langle \rangle$  the average. The nice feature of this quantity is that it allows to cancel differential phase errors between sub-pupils since they cancel each other out according to Eq.(1):

$$\text{CP}_{nn'n''} = \arg(\mu_{nn'n''}) = \psi_{nn'} + \psi_{n'n''} - \psi_{n''n'}, \quad (3)$$

The CP measurements are then fitted to a model to estimate physical parameters of the observed object.

At the Subaru Telescope, FIRST already showed that it could detect a companion below the diffraction limit (18 mas @700nm). Indeed, in the  $\alpha$  Equ binary system, a companion was detected with at a separation of around  $10.1 \pm 0.1$ mas, or almost half of the telescope diffraction limit. These data are still under analysis and are not shown in this proceeding.

#### 3.2 Science with GLINT

A typical image obtained with GLINT (here, on  $\alpha$  Boo) is shown Fig. 4-left. We see the 16 outputs of the integrated optics chip previously described. The red arrows point at two null outputs, where the light is cancelled.

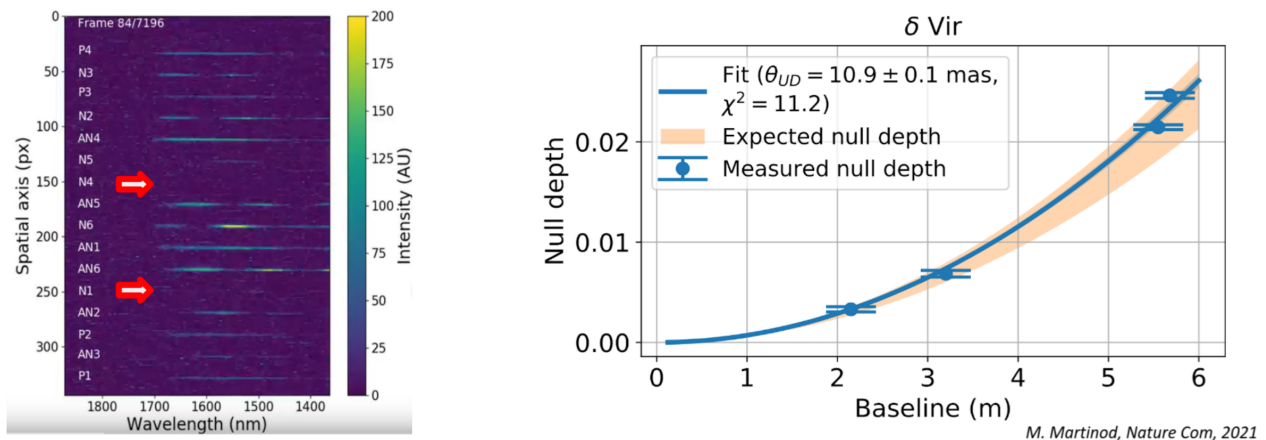


Figure 4. Left : GLINT image of  $\alpha$  Boo containing the 16 outputs. Red arrows point to null outputs. Right: Evolution of the null depth as a function of the baseline length in the case of  $\delta$  Virgo observation.<sup>18</sup> The expected null depth, from literature, is in orange. The measured null depth and fit providing the diameter  $\theta_{UD}$  estimation is in blue.

The data reduction pipeline is extensively explained and described in a previous article<sup>18</sup> hence we will just present one of the main GLINT result on Subaru here (more characterization and on-sky results can be found in the previous article<sup>18</sup>). GLINT was used to measure the diameter of  $\delta$  Virgo. Fig. 4-right shows the evolution of the null depth as a function of the baseline length, for the 4 baselines. The expected null depth from literature is plotted in orange, for a diameter between 9.86 and 11.3mas. The reason why the null depth increases with the baseline length is that the star limb is detected. This is what will allow here to measure the star diameter. We can see that the measured null depths and the fit match perfectly the expectation, estimating a diameter  $\theta_{UD}$  of  $10.9 \pm 0.1$ mas, assuming a uniform-disk star model. This well below the diffraction limit of the telescope (40mas @ 1550nm).

## 4. INTERFEROMETRIC WAVEFRONT SENSING

### 4.1 Context : measure discontinuities in the pupil phase (e.g. the Island Effect)

High contrast imaging systems kept on improving their capabilities to push down the achievable contrast. Under good conditions, achievable contrast with the SCEXAO/CHARIS imager<sup>10</sup> can go down to almost  $10^{-6}$  at about half an arcsecond.<sup>19</sup> However, the infamous Island Effect<sup>20,21</sup> (IE) limits achievable contrast. The IE can be divided in two categories of cause for the wavefront degradations: on one hand the spider-induced discontinuities of the pupil creates differential pistons not well seen by the WFS and therefore not well controlled (also named petalling or disconnectedness). On the other hand, the presence of the spiders creates, under some circumstances described hereafter, the Low Wind Effect (LWE). The LWE refers to a thermal effect (see Fig. 5-left). The temperature differential between the ambient air and the spiders ( $T_{spider} < T_{air}$ ) induces radiative exchanges: the air gets cooler near the spider (on Fig. 5-left warmer air is in red, cooler air is in blue). This creates a refractive index gradient near the spiders that induces local delays of the wavefront. This phenomenon occurs especially when the wind speed is low (typically below 3m/s), as the colder air is not blown away, and is to the best of our knowledge not detected by traditional WFS such as the Pyramid or the Shack-Hartmann.

The effect on the pupil phase was highlighted on the VLT/SPHERE.<sup>20</sup> Using the ZELDA Wavefront Sensor, it was possible to convert the pupil phase into an intensity map. It showed that the LWE creates differential Piston, Tip and Tilt errors in each quadrant of the pupil (one quadrant being delimited by the telescope spider). Fig. 5-right shows a focal plane image obtained with SCEXAO/VAMPIRES, where we can see the splitting of the Point Spread Function (PSF).

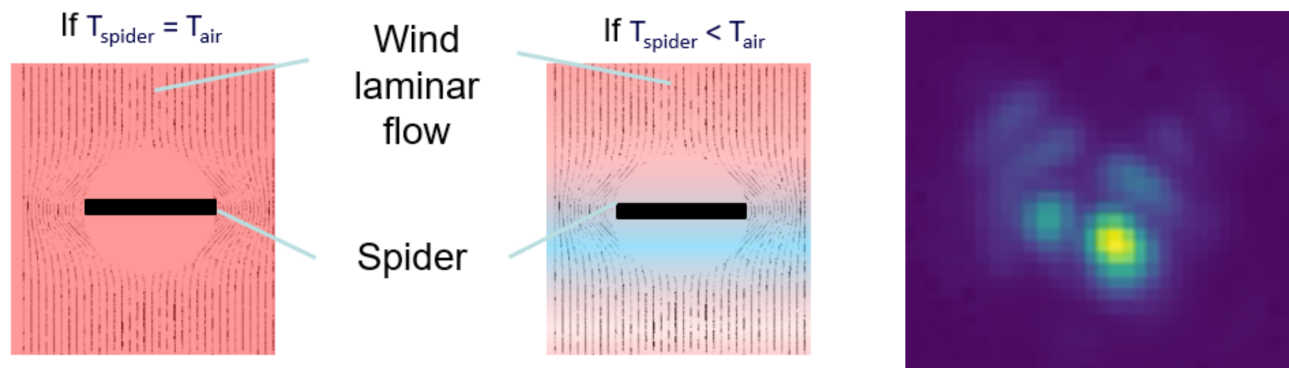


Figure 5. Left : The Low Wind Effect is caused by radiative exchanges between the spiders and the ambient air. Warmer air, in red, gets cooler, in blue, when passing across the cold spider. Right : Image obtained with the SCEXAO/VAMPIRES camera, in the presence of Low Wind Effect : the Point Spread Function splits.

Many techniques were developed or are being investigated on SCEXAO to measure and correct for the Island Effect, including focal plane wavefront sensing.<sup>21</sup> A novel method is currently under development : the interferometric Wavefront Sensing (iWFS). Since single aperture interferometers naturally measure relative phase between sub-pupils, they are the perfect candidates to measure phase discontinuities in the pupil.<sup>22</sup> Moreover, coupled with a spectrograph, these iWFS have a wavelength resolution. We now present preliminary and promising tests using FIRST and GLINT as iWFS.

## 4.2 Wavefront sensing with FIRST

We explained in Sec. 3.1 that we estimate the complex coherence terms for each baseline in order to compute the CPs. Doing so, we get rid of the  $\Delta\Phi_{nn'}$  differential piston terms from Eq.(1). For interferometric wavefront sensing purposes, these terms are the ones that we are interested in. Since the IE manifestation is differential Piston between quadrants, it should be included in the  $\Delta\Phi_{nn'}$  terms of baselines composed by sub-pupils from different quadrants. We first start to plot the OPD as a function of wavelength for 28 baselines issued from 8 sub-pupils, extracted from one frame (Fig. 6) obtained on Arcturus. Only one of the fiber sets is currently in use, minus one sub-pupil because of hardware issue on the MEMS (a broken segment). Fig. 6 shows that the baseline OPD (in green, limited between the blue  $\pm\lambda/2$  plots) is severely wrapped for many baselines. This is due to very large (several microns) static OPD between the hand-path length matched single mode extension fibers.

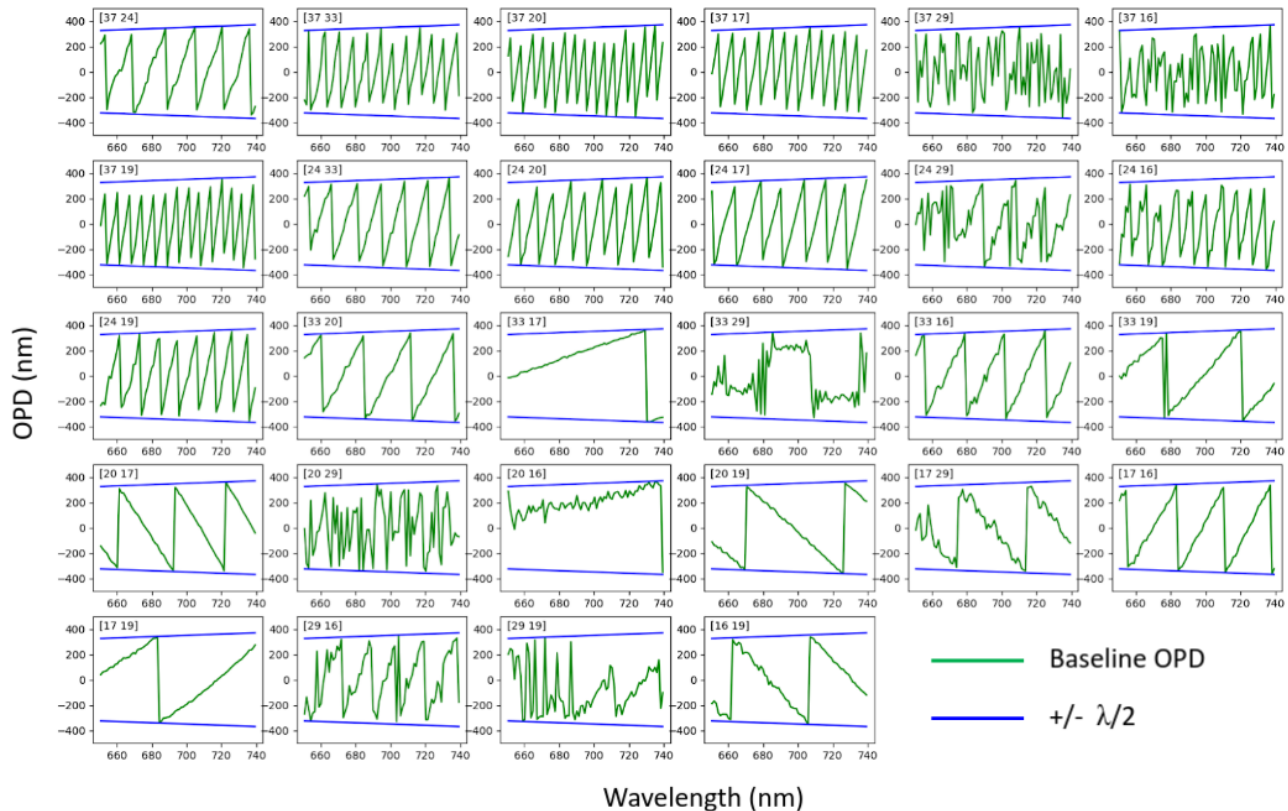
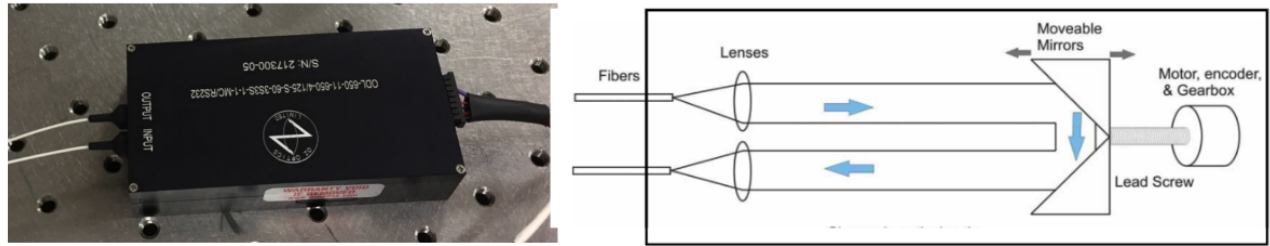


Figure 6. Graphs of the OPD as a function of the wavelength for 28 baselines, during the observation of Arcturus. The green curve is the baseline OPD and the blue curves are the  $\pm\lambda/2$  limits. The numbers in each sub-graph top left corner corresponds to the associated MEMS segments of the sub-pupils.

To reduce the large static OPD, we installed fibered Optical Delay Lines (ODLs). These ODLs allow to reduce the OPD between the fibers. Their principle is showed on Fig. 7. In addition, and to compensate for dynamic OPD induced by fibers stability, we installed a metrology source for FIRST. This metrology is composed by 4 lasers at 642, 785, 848 and 856 nm. Each of the metrology channels is superimposed and injected in parallel to the science light. This will allow to discriminate the OPD coming from the fibers. An example of an image obtained with FIRST using the SCEXAO internal calibration source superimposed with the metrology source is shown Fig. 8. We acquired on-sky data on Vega, on July 13th 2021, using the ODLs and the metrology setup. During the acquisition, we applied static Low Wind Effect phase maps on the SCEXAO deformable mirror. Data reduction is still on-going, and we are facing some technical difficulties, especially in terms of chromatic dispersion (coming from the newly installed fibered ODLs). Therefore, we do not have results to present here.

However, *V. Deo*<sup>22</sup> did some similar on-sky tests, on the Near-IR bench, using an aperture mask. He obtained some promising results, and showed that SAM could be used as an iWFS to correct for the Low Wind Effect in close loop. These results are very promising for FIRST that aims to do similar correction, with the addition of having spectral dispersion capabilities.



Courtesy: OzOptics

Figure 7. Optical Delay Lines picture (left) and principle (right).

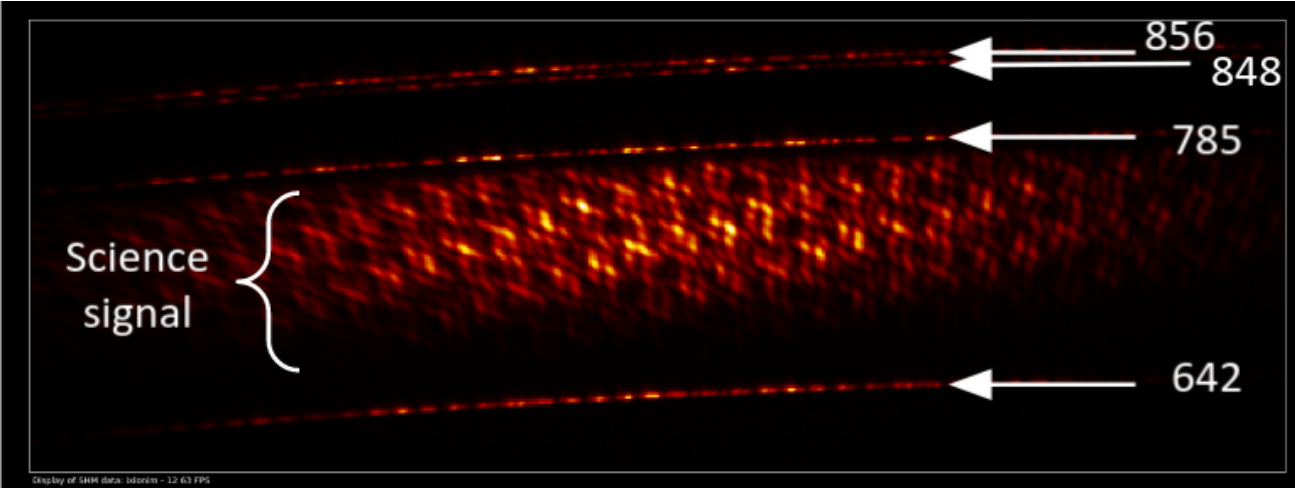


Figure 8. Image obtained on SCEXAO calibration SuperK source, superimposed with the metrology.

### 4.3 Wavefront sensing with GLINT

We show again the typical image obtained with GLINT on Fig. 9-left. The green arrows show the outputs that can be used for monitoring the residual optical aberration to calibrate how much starlight is left in the *null outputs*. Fig. 9-right shows data extracted from *null* (blue) and *anti-null* (orange) outputs, on AlfBoo (June 6th 2020). We can see the intensity in the outputs as a function of time (frames). The swap between the two outputs (two events, arounds frames 150 and 250) occurred during a LWE episode. This significant signature shows that it should be possible to monitor and feed this information in real-time to upstream deformable mirror for correction. More investigations are currently undertaken in order to use GLINT to extract differential piston between sub-apertures.

## 5. CONCLUSION

We presented two single telescope spectro-interferometers installed at the Subaru Telescope : FIRST, in the Visible, and GLINT, in the Near-IR. We explained how preliminary on-sky tests with FIRST allowed to resolve the  $\alpha$  Equ binary system, with an estimated separation of  $10.1 \pm 0.1$  mas using closure phase model fitting. This is almost half of the theoretical limit of resolution of the Subaru Telescope in the Visible. The nuller GLINT was able to estimate the diameter of  $\delta$  Virgo:  $10.9 \pm 0.1$ mas, which is a quarter of the telescope spatial resolution in the Near-IR. Both these results are in accordance with the literature, and demonstrate the capability of the two

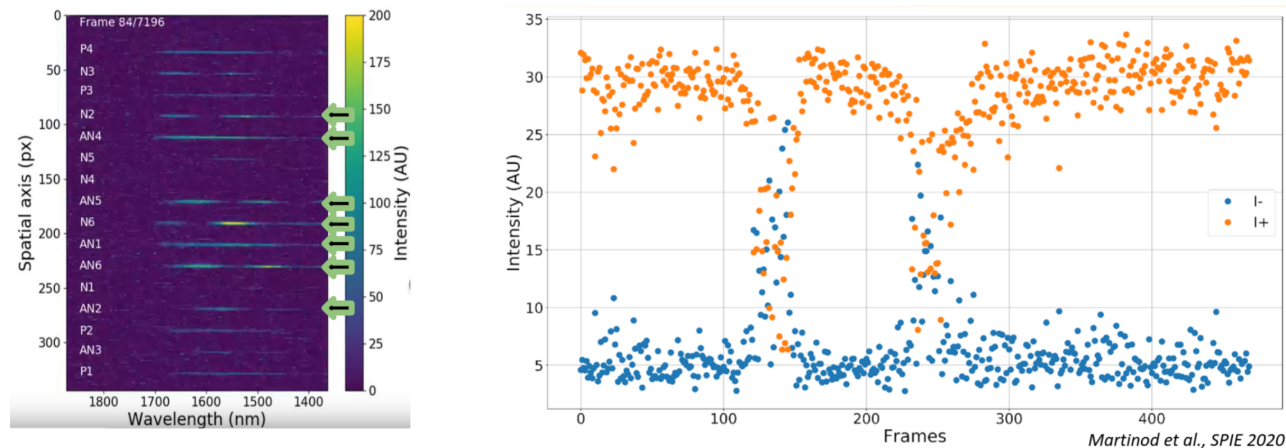


Figure 9. Left: GLINT image obtained on  $\alpha$  Boo. The green arrows point to the fringe tracking outputs. Right : Intensity of a null and anti-null outputs, respectively in blue and orange, as a function of time. Inversion of the outputs can be noticed around frames 150 and 250, due to the Low Wind Effect.

instruments to provide measurements below the diffraction limit of the telescope. We then presented the concept of interferometric Wavefront Sensing. Using FIRST and GLINT, it is possible to measure the discontinuities of the pupil phase thanks to the sub-pupil differential phase measurements. This is particularly interesting since it can help tackling down the Island Effect. It could even potentially help with segmented telescope cophasing. In the near future, the FIRST instrument will upgrade its recombination scheme and use integrated chip optics (similarly to GLINT). The two instruments are showing that it will be possible to do measurements well below the diffraction limit of a single telescope while providing precious information to improve the wavefront quality, using a compact integrated photonic chip.

## ACKNOWLEDGMENTS

The development of FIRST was supported by Centre National de la Recherche Scientifique CNRS (Grant ERC LITHIUM - STG - 639248). The development of SCEXAO was supported by the Japan Society for the Promotion of Science (Grant-in-Aid for Research #23340051, #26220704, #23103002, #19H00703 & #19H00695), the Astrobiology Center of the National Institutes of Natural Sciences, Japan, the Mt Cuba Foundation and the director's contingency fund at Subaru Telescope. GLINT work was supported by the Australian Research Council Discovery Project DP180103413. Critical fabrication for GLINT was performed in part at the OptoFab node of the Australian National Fabrication Facility utilising Commonwealth as well as NSW state government funding. S. Gross acknowledges funding through a Macquarie University Research Fellowship (9201300682) and the Australian Research Council Discovery Program (DE160100714). N. Cvetojevic acknowledges funding from the European Research Council (ERC) under the European Union's Horizon 2020 research and innovation program (grant agreement CoG - 683029). The authors wish to recognize and acknowledge the very significant cultural role and reverence that the summit of Maunakea has always had within the indigenous Hawaiian community. We are most fortunate to have the opportunity to conduct observations from this mountain.

## REFERENCES

- [1] Mayor, M. and Queloz, D., "A jupiter-mass companion to a solar-type star," *Nature* **378**(6555), 355–359 (1995).
- [2] Seager, S., [*Exoplanet atmospheres*], Princeton University Press (2010).
- [3] Pascucci, I., Mulders, G., Fernandes, R., and Gould, A., "Exoplanet populations beyond kepler," in [*American Astronomical Society Meeting Abstracts# 233*], **233**, 227–05 (2019).
- [4] Lacour, S., Tuthill, P., Amico, P., Ireland, M., Ehrenreich, D., Huelamo, N., and Lagrange, A.-M., "Sparse aperture masking at the vlt-i. faint companion detection limits for the two debris disk stars hd 92945 and hd 141569," *Astronomy & Astrophysics* **532**, A72 (2011).

- [5] Perrin, G. S., Lai, O., Lena, P. J., and du Foresto, V. C., “Fibered large interferometer on top of mauna kea: Ohana, the optical hawaiian array for nanoradian astronomy,” in [*Interferometry in Optical Astronomy*], **4006**, 708–714, International Society for Optics and Photonics (2000).
- [6] Martin, G., Bhuyan, M., Troles, J., D’Amico, C., Stoian, R., and Le Coarer, E., “Near infrared spectro-interferometer using femtosecond laser written gls embedded waveguides and nano-scatterers,” *Optics express* **25**(7), 8386–8397 (2017).
- [7] Jovanovic, N., Guyon, O., Kotani, T., Kawahara, H., Hosokawa, K., Lozi, J., Males, J., Ireland, M., Tamura, M., Mawet, D., et al., “Developing post-coronagraphic, high-resolution spectroscopy for terrestrial planet characterization on elts,” *arXiv preprint arXiv:1712.07762* (2017).
- [8] Minowa, Y., Hayano, Y., Oya, S., Watanabe, M., Hattori, M., Guyon, O., Egner, S., Saito, Y., Ito, M., Takami, H., et al., “Performance of subaru adaptive optics system ao188,” in [*Adaptive Optics Systems II*], **7736**, 77363N, International Society for Optics and Photonics (2010).
- [9] Lozi, J., Jovanovic, N., Guyon, O., Chun, M., Jacobson, S., Goebel, S., and Martinache, F., “Visible and near-infrared laboratory demonstration of a simplified pyramid wavefront sensor,” *Publications of the Astronomical Society of the Pacific* **131**, 044503 (mar 2019).
- [10] Currie, T., Brandt, T. D., Uyama, T., Nielsen, E. L., Blunt, S., Guyon, O., Tamura, M., Marois, C., Mede, K., Kuzuhara, M., Groff, T. D., Jovanovic, N., Kasdin, N. J., Lozi, J., Hodapp, K., Chilcote, J., Carson, J., Martinache, F., Goebel, S., Grady, C., McElwain, M., Akiyama, E., Asensio-Torres, R., Hayashi, M., Janson, M., Knapp, G. R., Kwon, J., Nishikawa, J., Oh, D., Schlieder, J., Serabyn, E., Sitko, M., and Skaf, N., “SCEXAO/CHARIS near-infrared direct imaging, spectroscopy, and forward-modeling of kappa and b: A likely young, low-gravity superjovian companion,” *The Astronomical Journal* **156**, 291 (nov 2018).
- [11] Norris, B., Schworer, G., Tuthill, P., Jovanovic, N., Guyon, O., Stewart, P., and Martinache, F., “The VAMPIRES instrument: imaging the innermost regions of protoplanetary discs with polarimetric interferometry,” *Monthly Notices of the Royal Astronomical Society* **447**, 2894–2906 (01 2015).
- [12] Huby, E., Perrin, G., Marchis, F., Lacour, S., Kotani, T., Duchêne, G., Choquet, E., Gates, E., Woillez, J., Lai, O., et al., “First, a fibered aperture masking instrument-i. first on-sky test results,” *Astronomy & Astrophysics* **541**, A55 (2012).
- [13] Norris, B. R. M., Cvetojevic, N., Lagadec, T., Jovanovic, N., Gross, S., Arriola, A., Gretzinger, T., Martinod, M.-A., Guyon, O., Lozi, J., Withford, M. J., Lawrence, J. S., and Tuthill, P., “First on-sky demonstration of an integrated-photonic nulling interferometer: the GLINT instrument,” *Monthly Notices of the Royal Astronomical Society* **491**, 4180–4193 (Jan. 2020).
- [14] Gibson, R. K., Oppenheimer, R., Matthews, C. T., and Vasisht, G., “Characterization of the C-RED 2: a high-frame rate near-infrared camera,” *Journal of Astronomical Telescopes, Instruments, and Systems* **6**, 011002 (Jan. 2020).
- [15] **Marc-Antoine Martinod**, Norris, B., Lagadec, T., Jovanovic, N., Cvetojevic, N., Gross, S., Arriola, A., Gretzinger, T., Withford, M. J., Guyon, O., Lozi, J., Lawrence, J. S., Tuthill, P. G., and Leon-Saval, S., “The first multi-baseline and multi-band, photonic nuller at the Subaru telescope: the GLINT nulling interferometer,” in [*Optical and Infrared Interferometry and Imaging VII*], Tuthill, P. G., Mérand, A., and Sallum, S., eds., **11446**, International Society for Optics and Photonics, SPIE (2020).
- [16] Tatulli, E., Millour, F., Chelli, A., Duvert, G., Acke, B., Utrera, O. H., Hofmann, K.-H., Kraus, S., Malbet, F., Mège, P., et al., “Interferometric data reduction with amber/vlti. principle, estimators, and illustration,” *Astronomy & Astrophysics* **464**(1), 29–42 (2007).
- [17] Huby, E., *Caractérisation de systèmes binaires par imagerie haute dynamique non redondante fibrée*, PhD thesis, Observatoire de Paris (2013).
- [18] Martinod, M.-A., Norris, B., Tuthill, P., Lagadec, T., Jovanovic, N., Cvetojevic, N., Gross, S., Arriola, A., Gretzinger, T., Withford, M. J., et al., “Scalable photonic-based nulling interferometry with the dispersed multi-baseline glint instrument,” *Nature communications* **12**(1), 1–11 (2021).
- [19] Currie, T., Brandt, T. D., Kuzuhara, M., Chilcote, J., Cashman, E., Liu, R. Y., Lawson, K., Tobin, T., Brandt, G. M., Guyon, O., Lozi, J., Deo, V., Vievard, S., Ahn, K., and Skaf, N., “A new type of exoplanet direct imaging search: a scexao/charis survey of accelerating stars,” *Proceeding SPIE, Optical Engineering + Applications*, Paper 11823–3 (2021).

- [20] Sauvage, J.-F., Fusco, T., Guesalaga, A., Wizinowitch, P., O'Neal, J., N'Diaye, M., Vigan, A., Grard, J., Lesur, G., Mouillet, D., et al., "Low wind effect, the main limitation of the sphere instrument," in [*Adaptive Optics for Extremely Large Telescopes 4-Conference Proceedings*], **1**(1) (2015).
- [21] Vievard, S., Bos, S. P., Cassaing, F., Currie, T., Deo, V., Guyon, O., Jovanovic, N., Keller, C. U., Lamb, M., Lopez, C., et al., "Focal plane wavefront sensing on subaru/scexao," in [*Adaptive Optics Systems VII*], **11448**, 114486D, International Society for Optics and Photonics (2020).
- [22] Deo, V., Vievard, S., Cvetojevic, N., Norris, B., Guyon, O., Lozi, J., Ahn, K., Huby, E., Jovanovic, N., Lacour, S., Martinache, F., Skaf, N., and Tuthill, P., "Wavefront sensing using non-redundant aperture masking interferometry: tests and validation on subaru/scexao," *Proceeding SPIE, Optical Engineering + Applications* , Paper 11823-39 (2021).